Days to weeks of syn-eruptive magma interaction: High-resolution geochemistry of the 2002-03 branched eruption at Mount Etna

Ruadhán Magee [a,*], Teresa Ubide [a], John Caulfield [a,b]

[a] *School of Earth and Environmental Sciences, The University of Queensland, 4072, QLD, Australia*
[b] *Central Analytical Research Facility, Queensland University of Technology, 4000, QLD, Australia*

ARTICLE INFO

ABSTRACT

Eruption onset, style and duration are governed, in part, by the movement and interaction of distinct magma bodies at depth. High-resolution investigation of erupted products can retrospectively inform our understanding of such processes and improve future interpretation of real-time monitoring signals. In 2002-03, Mount Etna (Italy) erupted two elementally and isotopically distinct magmas simultaneously, providing a unique opportunity to explore magma transport and evolution through complex, well-documented and monitored volcanic activity. In this study, melt chemistry (groundmass fraction as opposed to whole-rock) and mineral zoning (X-ray fluorescence mapping and electron microprobe) are treated as separate recorders of magma history tracking syn- and pre-eruptive processes, respectively. Elemental mapping of entire thin sections revealed a largely antecrystic, hybrid crystal cargo hosting reverse-zoned clinopyroxene and olivine, supporting extensive magma mixing in southern flank conduits. Antecryst-free groundmass chemo-stratigraphies reveal melt compositional variations on timescales of days to weeks. In agreement with previous whole-rock studies, we find that during the early-middle stages of activity, melt erupted on the southern flank was rich in MgO, CaO, Cr, Ni, and radiogenic-Sr, and depleted in Al_2O_3, Na_2O, La, Zr, relative to its north-eastern counterpart. In addition, high resolution tracking of melt composition reveals a progressive shift to increasingly evolved compositions over the course of the S-rift eruption. A corresponding shift in $^{87}Sr/^{86}Sr$ isotope ratios (0.70366 to 0.70358) across the same period implies progressive mixing of isotopically distinct magmas as the main driver of the observed compositional change. In contrast, NE-rift products lack evidence of mixing in both melt and mineral records, in agreement with previous work suggesting geodynamically controlled draining of shallow, isolated magma pockets. Comparing recharge-to-eruption timescales derived from mineral zonation with real-time monitoring data and groundmass compositional data, we show that the onset of magma mixing in the S-rift coincided with a deep seismic event (8-18 km) and was followed by the ascent of undegassed magma approximately 2 months before eruption onset. Finally, we demonstrate that high-resolution temporal changes in melt composition, approached through melt geochemistry, are closely linked to eruption intensity and SO_2 emission. We suggest that composition and explosivity on the southern rift fluctuated in response to multiple phases of recharge-mixing-hybridisation between undegassed 'eccentric' magma and a degassed resident magma at 3-5 km depth. Our results highlight that high-resolution geochemistry can improve our understanding of deep magmatic processes driving eruption onset, duration and intensity. Rapid analysis of melt composition integrated with traditional monitoring approaches could improve future hazard response at Mount Etna and active volcanoes globally.

© 2021 Elsevier B.V. All rights reserved.

1. Introduction

Through the investigation of a volcano's eruptive products, the architecture of its internal plumbing system can be better under-stood. Details of pre-eruptive magma storage, transport and evolution can then act as a crucial guide to volcano monitoring efforts, assessments of explosivity and hazard potential (Costa et al., 2020). During the 2018 Kilauea eruption in Hawaii, Gansecki et al. (2019) demonstrated the power of rapid geochemical analysis as a real-time monitoring tool, measuring variation in whole-rock chemistry within hours of eruption and informing an appropriate hazard response. However, whole-rock material comprises two separate, and
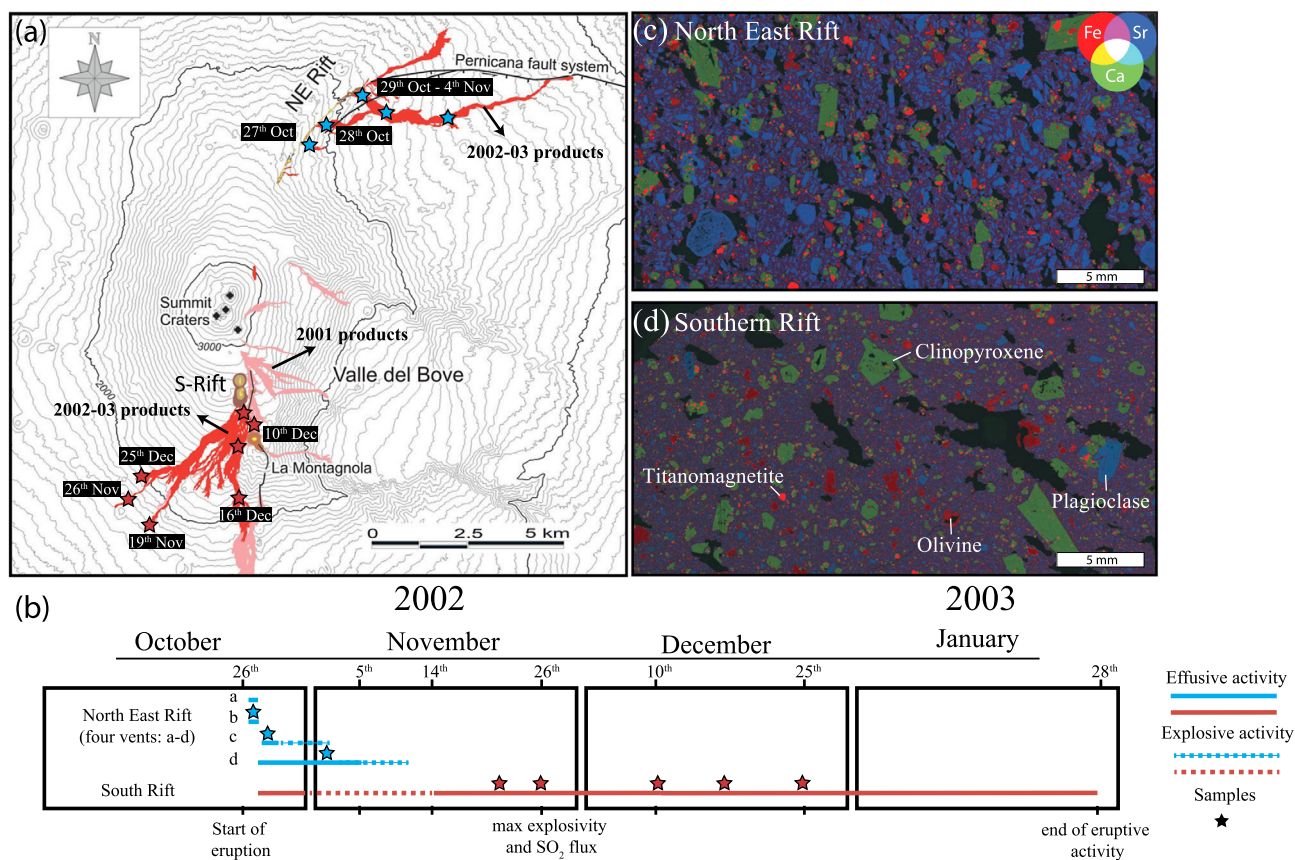
Fig. 1. (a) Map showing the extent of 2002-03 NE-rift and S-rift lava flows (in red; adapted from Andronico et al., 2005). 2001 products are depicted in pink. Sample locations are marked by blue stars (NE-rift) and red stars (S-rift). (b) Timeline of events during the 2002-03 eruption. (c, d) Three-element XFM maps (Fe, Ca, Sr) of representative thin sections of (c) NE-rift magma and (d) S-rift magma. All major mineral phases are shown including plagioclase (blue), clinopyroxene (green), olivine (dark red) and titanomagnetite (bright orange). Vesicles are black. (For interpretation of the colours in the figure(s), the reader is referred to the web version of this article.)

sometimes conflicting, petrological recorders of magma history: melt and minerals. A protracted record of magma storage is preserved in mineral zonation (Davidson et al., 2007; Ginibre et al., 2007), and many studies show that minerals are not in equilibrium with their final host magma (Armienti et al., 2007; Ganne et al., 2018). Subtle changes in melt composition may, therefore, be obscured in crystal-rich magma to the point of being undetectable. Full disentanglement of these coexisting records could improve the tracking of such changes but requires a high-resolution geochemical approach that can extract information from melts (free of disequilibrium crystals) and individual crystal zones. In this study, we combine temporal analysis of groundmass aliquots (fine grained matrix + microphenocrysts up to 0.5 mm), carefully hand-picked from whole-rock material, with targeted analysis of mineral populations at the scale of entire thin sections, to reveal both syn- and pre-eruptive processes.

The landmark 2002-03 eruption of Mount Etna is an ideal event through which to track the movement and interaction of individual batches of magma through an active plumbing system. The eruption began with the simultaneous opening of two of Etna's most active rift systems; the southern rift (S-rift) and the north-east rift (NE-rift) (Fig. 1). Two distinct magmas emerged along these known conduits highlighting the complexity of Etna's active system (Clocchiatti et al., 2004; Andronico et al., 2005). The magma erupted on the NE-rift is considered typical of Etna's central-conduits which feed most of the volcano's eruptive activity (Clocchiatti et al., 2004). In contrast, magma erupted on the S-rift is thought to bypass these central-conduits, ascending rapidly from depth. Such eruptions are termed 'eccentric' and have occurred only three times during the current eruptive period (1974, 2001

lower vents and 2002-03 S-rift; Corsaro et al., 2009). However, the connectivity of these pathways and resulting level of interaction between the two identified magmas, if any, remains unclear, and is crucial to understanding the translation of subvolcanic processes to subaerial eruptive hazards. Here we investigate the temporal heterogeneity of lava emitted on both flanks during the 2002-03 eruption, tracking the evolution of minerals and melts on timescales of days to weeks. Additionally, we show that changes in melt and mineral composition in S-rift magma coincide with real-time pre- and syn-eruptive monitoring parameters, highlighting their potential to assist in eruption forecasting and response.

2. The philosophy

From mantle source to surface, an ascending body of magma must traverse the overlying crust (20-30 km at Etna), potentially ponding, mixing and crystallising en-route to eruption (Cashman et al., 2017). This journey involves inevitable interaction with other unerupted magma bodies, themselves varying in composition and crystal content, i.e. the magma mush column (Marsh, 2006; Cashman et al., 2017). In fact, based on the amount of SO_2 emitted between the years 2002 and 2006, it is estimated that 24% of the magma supplied to Etna's plumbing system remained un-erupted (Steffke et al., 2011). It is not surprising then that residual crystals of varying ages and origins are commonly entrained in ascending melts and brought to the surface as antecrysts, in a diverse crystal cargo (Armienti et al., 2007; Ganne et al., 2018). Whole-rock analyses of antecryst-bearing volcanic rocks therefore do not represent the composition of erupted melt, but rather a combination of melt

and crystals which may or may not share a common origin (Reubi and Blundy, 2009; Ubide et al., 2014).

Our approach considers melt composition and crystal cargo as separate recorders of magmatic history. We apply high-resolution mineral (pre-eruptive storage) and groundmass (late-stage melt) geochemistry to a set of temporally constrained samples and compare them with whole-rock analyses of original bulk rocks (unseparated aliquots from the same samples) and literature whole-rock data. By physically removing the magma's crystal cargo, avoiding mixed mineral/melt signals, we aim to reliably track syn-eruptive changes in melt composition throughout the eruption.

Through hand-picking, it is neither possible nor desirable to remove all crystal phases. Abundant microlite and microphenocryst crystallisation typically occurs in the final stages prior to eruption (whereupon degassing results in a rapid burst of nucleation; Armienti et al., 2007) and these crystals are likely to be in equilibrium with the final melt. The removal of such crystals, or analysis of residual melt (i.e. matrix glass), would result in unrealistically evolved compositions (Cashman, 1992), unrepresentative of pre-eruptive melt. The aim of 'groundmass' picking is to avoid the accumulation of large, disequilibrium crystal phases, whose inclusion in the bulk analysis may modify - 1) the measured primitivity of the melt (major and trace elements), and - 2) its isotopic composition.

In addition, our approach to the study of composition and zoning in the crystal cargo minimises bias. By obtaining compositional maps of entire thin sections we identify major populations, antecrysts and outliers, some of which may otherwise be overlooked. Selected minerals are targeted for more detailed analysis of pre-eruptive magma storage.

3. Background

3.1. Eruptive activity at Mount Etna

Following the major eruptive activity of the seventeenth century, which culminated with the destructive 1669 eruption (Magee et al., 2020) the composition of Mount Etna magma remained relatively constant, recording only a slight progressive increase in alkali elements (Armienti et al., 2004; Corsaro and Pompilio, 2004). The volcano erupted porphyritic, plagioclase-rich hawaiites (Viccaro and Cristofolini, 2008) interpreted as having drained well-established central-conduit magma chambers (Corsaro et al., 2009). Beginning in 1974, however, the first appearance of an 'eccentric' plagioclase-poor magma marked a turning point in magma composition and eruption dynamics (Kamenetsky et al., 2007; Corsaro et al., 2009). This new, more primitive magma was also characterised by elevated concentrations of alkalis (Cs, Rb, K) and more radiogenic Sr isotopic compositions (Tanguy et al., 1997), suggesting a first-order shift in the mantle source feeding the volcano (Viccaro and Cristofolini, 2008).

Over the last 50 years, the frequency of eruptions at Mount Etna has increased dramatically, coupled with a rise in explosivity (Kamenetsky et al., 2007). The spectacular paroxysms of February-March 2021, ongoing at the time of writing, powerfully demonstrate the continuation of this trend. It is widely accepted that the volatile-rich eccentric magma has been invading, mixing with and progressively replacing resident central-conduit magma since its first appearance in 1974 (Métrich et al., 2004; Corsaro et al., 2007; Ubide and Kamber, 2018), if not earlier. While broad compositional and isotopic differences between pre-1970 and post-1970 magma are pronounced (Viccaro and Cristofolini, 2008), they do not highlight eruption-specific magmatic interactions which are often key drivers of eruption (Ubide and Kamber, 2018). The identification of well-constrained isotopic endmembers within the plumbing system (Clocchiatti et al., 2004; Armienti et al., 2007; Corsaro et al.,

2013) presents a unique opportunity to investigate magmatic interaction at the eruption scale. Subtle magmatic changes in elemental and isotopic composition within a single event, which may influence changes in eruption intensity and hazard level, add critical nuance to the wide range of compositional values observed in post-1970 magmas.

3.2. The 2002-03 eruption: characteristics and chronology

Two magmas began erupting nearly simultaneously in October 2002. Not only were they spatially, texturally and compositionally distinct (Fig. 1c, d), but also characterised by markedly different eruption dynamics (Clocchiatti et al., 2004; Di Renzo et al., 2019). Highly porphyritic, plagioclase-rich magma, typical of the post-1970 central-conduits (Clocchiatti et al., 2004; Corsaro et al., 2007) emerged from a series of vents along the NE-rift (vents 3a, 3b, 3c and 3d; Andronico et al., 2005) (Fig. 1a). Opening sequentially, the NE-rift vents produced four easily distinguishable lava flows (Fig. 1a), during activity that lasted a total of 9 days (26th October- 5th November). Vents 3a, 3b and 3c were characterised by intense, short-lived strombolian activity and minor effusive activity, while vent 3d produced an extensive lava flow that destroyed the tourist facility at Piano Provenzana (Andronico et al., 2005). In contrast, plagioclase-poor magma with lower overall porphyricity emerged on the southern rift alternating between two main vents at 2,750 m and 2,800 m above sea level. The eruption lasted almost 3 months (26th October - 28th January; Fig. 1b) and is considered one of the most explosive events in recent history (1329-2003; Andronico et al., 2005). The style and intensity of eruption varied frequently. Distinct peaks in explosivity coincided with peaks in SO_2 emission and were preceded by the onset of effusive output, notably between the 14th and 28th of November, during which time the highest SO_2 value ever measured at Mount Etna ($\sim$29,000 t/d; Andronico et al., 2005) was recorded. This peak in activity was followed by a progressive waning in explosivity towards the end of the eruptive period (10[th] of December - January 28[th]), accompanied by low SO_2 output ($\sim$4,000-8,000 t/d; Andronico et al., 2005; Spilliaert et al., 2006). Here we focus on the effusive products emitted throughout the eruption (Fig. 1b), correlating changes in melt and mineral chemistry with eruptive style and perturbations in real-time monitoring data.

4. Methods

4.1. Samples

This study includes samples of 'a'ā lava emitted from the NE-rift (8 samples) and S-rift (13 samples) (Fig. 1b). In the NE-rift, we sampled products from vents 3b, 3c and 3d (27th October – 5th November). Vent 3a, the earliest erupted lava (26th October – 31st October), is thought to represent an isolated pocked of pre-1970 magma (Ferlito et al., 2009) and is not discussed further in this study. Samples collected from the S-rift (19th November – 25th December) include all major episodes of effusive activity, excluding the earliest erupted products (28th October – 18th November) which were rapidly buried by subsequent lava flows. Sample eruption dates were assigned based on INGV reports and published lava field maps (Andronico et al., 2005). Sampling locations are shown in Fig. 1 and the corresponding GPS coordinates are reported in Table C.1, Appendix C.

4.2. Tracking melt composition through time

Samples were crushed into 1-2 mm fragments and the groundmass fraction carefully hand-picked from whole-rock material using a tweezers and light microscope. Phenocrysts of up to 0.5 mm

were considered an integral part of the pre-eruptive melt composition. Analysis of crystal size distributions (CSD) in Etnean magma has shown that both clinopyroxene and plagioclase crystals of 0.5 mm or less are related to final magma ascent (Armienti et al., 1994; Orlando et al., 2008). The demarcation is slightly smaller for olivine (<0.3 mm); however, olivine is not an abundant microcrystalline phase (Table C.2, Appendix C). The 0.5 mm cut-off agrees with clinopyroxene zoning. In S-rift magma, crystals of 0.5 mm size, and in some instances even larger, have Cr-rich zones at their cores indicating late-stage crystallisation following magma recharge. We acknowledge that hand-picking cannot remove all crystals >0.5 mm in size; some portion of disequilibrium crystals will remain. A more detailed discussion of groundmass picking and its limitations can be found in Appendix A.1.

Selected whole-rock samples were also prepared for analysis for comparison with the results of groundmass chemistry.

4.3. Chemical analysis

Major element analysis was conducted by Inductively Coupled Plasma-Optical Emission Spectrometry (ICP-OES) in the Environmental Geochemistry Laboratory at the University of Queensland (UQ-EGL). In preparation for trace element and Sr isotope analysis, rock powders were dissolved using mixtures of double distilled concentrated HNO_3 and HF and 10% aqua regia in ultra-clean 20 ml Teflon beakers in the Radiogenic Isotope Facility at The University of Queensland (UQ-RIF). An aliquot of sample solution was taken for trace element analysis. Samples were diluted 3000x and spiked at 6 ppb with a multi-element standard. Solutions were analysed on an Agilent 7900 Inductively Coupled Plasma-Mass Spectrometer (ICP-MS) in gas (He) and no gas modes in the Environmental Geochemistry Laboratory, The University of Queensland. In house solutions of W2a, BHVO-2 and BIR were used for calibration purposes, with procedural digestions of JB-2 and BHVO-2 serving as quality monitors. Accuracy and precision were typically better than 5%. The remaining sample solution was passed through Sr Spec resin to isolate the Sr fraction. Samples were diluted to 40 ppb and analysed on a Nu Instruments Multi Collector-ICP-MS in the Radiogenic Isotope Facility, The University of Queensland. Samples were bracketed with the NBS987 Sr standard. Uncertainty on $^{87}Sr/^{86}Sr$ isotope ratios ($\pm 2\sigma$) was between 8×10^{-6} and 9×10^{-6} for all analyses.

A second analysis of key trace elements (Cr, Ni) carried out by ICP-MS at the UQ-EGL was integrated with the initial dataset (Cr: Fig. 3b) and validated the observed compositional trends. Full details of analytical methods are provided in Appendix A1-4 and data are available in Table C.3 of Appendix C.

4.4. Crystal cargo analysis

Three samples from the NE-rift and three from the S-rift were selected for x-ray fluorescence microscopy (XFM) mapping at the Australian Synchrotron. Polished thin sections were mapped using an energy of 19.1 keV. To allow rapid visualisation of elemental distributions (Fe, Ca, Sr, Mn, Ti, Ni), we used a spot size of 10 μm, a scan speed of 5 mm/s (2 msec/pixel) and a slit size of 20 μm. Smaller areas of interest were subsequently mapped with a reduced beam size of 2 μm, a scan speed of 1.5 mm/s (1.33 msec/pixel) and a slit size of 20 μm, for more detailed imaging. XFM elemental maps of entire thin sections were used to identify distinct populations of each mineral type (Ca-Fe for clinopyroxene, Ca-Sr for plagioclase and Fe-Mn for olivine) for targeted analysis. The abundance of each population was counted using the colour thresholding function in ImageJ. Elemental data extracted from XFM maps are considered semi-quantitative. However, the colour scale of each map was cross calibrated with quantitative electron microprobe data to allow for accurate comparison of mineral populations across samples. For each thin-section, major element core-rim transects were conducted on a representative member of each distinct olivine and clinopyroxene population. Full electron microprobe methodology is found in Appendix A5-6 and mineral data are available in Tables C.4 and C.5 of Appendix C.

5. Results

5.1. Petrology of NE-rift vs S-rift samples

Mineral modes highlight obvious textural differences between the NE-rift and S-rift lavas (Table C.2), characteristics that are well documented in the literature (Andronico et al., 2005; Clocchiatti et al., 2004; Giacomoni et al., 2014). Those erupted on the southern flank are less porphyritic (porphyritic index, PI: 3-10 vol. %; calculated by point counting on a vesicle free basis, including crystals >1 mm) than those of the NE-rift (PI: 7-17 vol. %), a feature that is principally reflected in the abundance of plagioclase phenocrysts (Giacomoni et al., 2014; Kahl et al., 2015; Di Renzo et al., 2019). The microphenocryst population (<1 mm) of both magmas differs even more starkly. The percentage of microphenocrysts in NE-rift groundmass (30-63 vol. %) greatly exceeds that of the S-rift (3-35 vol. %), again mostly reflected in the abundance of plagioclase microphenocrysts in the NE rift (Fig. 1c, d). These data serve only as a general indication of the crystal content in each magma and do not refer specifically to the picked fraction. We use the terms microphenocryst and phenocryst in reference to crystal size only, not origin.

Compositional variation in major elements, trace elements and Sr isotope ratios differentiate NE-rift and S-rift groundmass into separate groups. Samples erupted on the S-rift show higher concentrations of MgO, CaO, Cr and Ni and lower concentrations of Al_2O_3 compared with the NE-rift (Fig. 2a-d), as noted by previous authors (Clocchiatti et al., 2004; Giacomoni et al., 2012; Di Renzo et al., 2019). All samples classify as trachybasalts in the total alkalis vs silica (**TAS**) diagram (Bas et al., 1986), but define two groups based on alkali content (Fig. 2e). S-rift samples fall below 6 wt. % $Na_2O + K_2O$ while those of the NE-rift plot both below and above 6 wt. % $Na_2O + K_2O$, suggesting heterogeneity in alkali elements in the erupted material (Ferlito et al., 2009).

5.2. Groundmass vs whole-rock compositions

There are significant differences in the major and trace element compositions of whole-rock and groundmass material for a given sample (Fig. 2). In our dataset, maximum differences of +23% MgO, +11% CaO, −27% Al_2O_3, +78% Cr and +52% Ni are observed in whole-rock samples relative to their corresponding groundmass. Furthermore, compositional variability within the S-rift groundmass, when compared with whole-rock data from this study and literature (collected from the same localities), is significantly lower (Fig. 3a, b, c). On the S-rift, a range of only 20 ppm chromium (19-39 ppm Cr) is observed in groundmass, while the same whole-rock samples from the same eruption period show a range of 38 ppm (41-79 ppm Cr). Reduced compositional variability in groundmass samples is observed for most major and trace elements (CaO, Al_2O_3, MgO, Ni; Figs. 2 and 3), particularly those compatible in the major mineral phases (clinopyroxene, plagioclase, olivine and Ti-magnetite). Hence, the difference in composition between whole-rock and groundmass is likely controlled by the porphyricity of the whole-rock samples as well as the relative abundance and composition of each mineral. While whole-rock samples analysed in this study (n=2) cover a small range of the compositional variation observed in the literature whole-rock, the range of porphyricity observed in all studied samples is highly variable. Table C.2 reveals
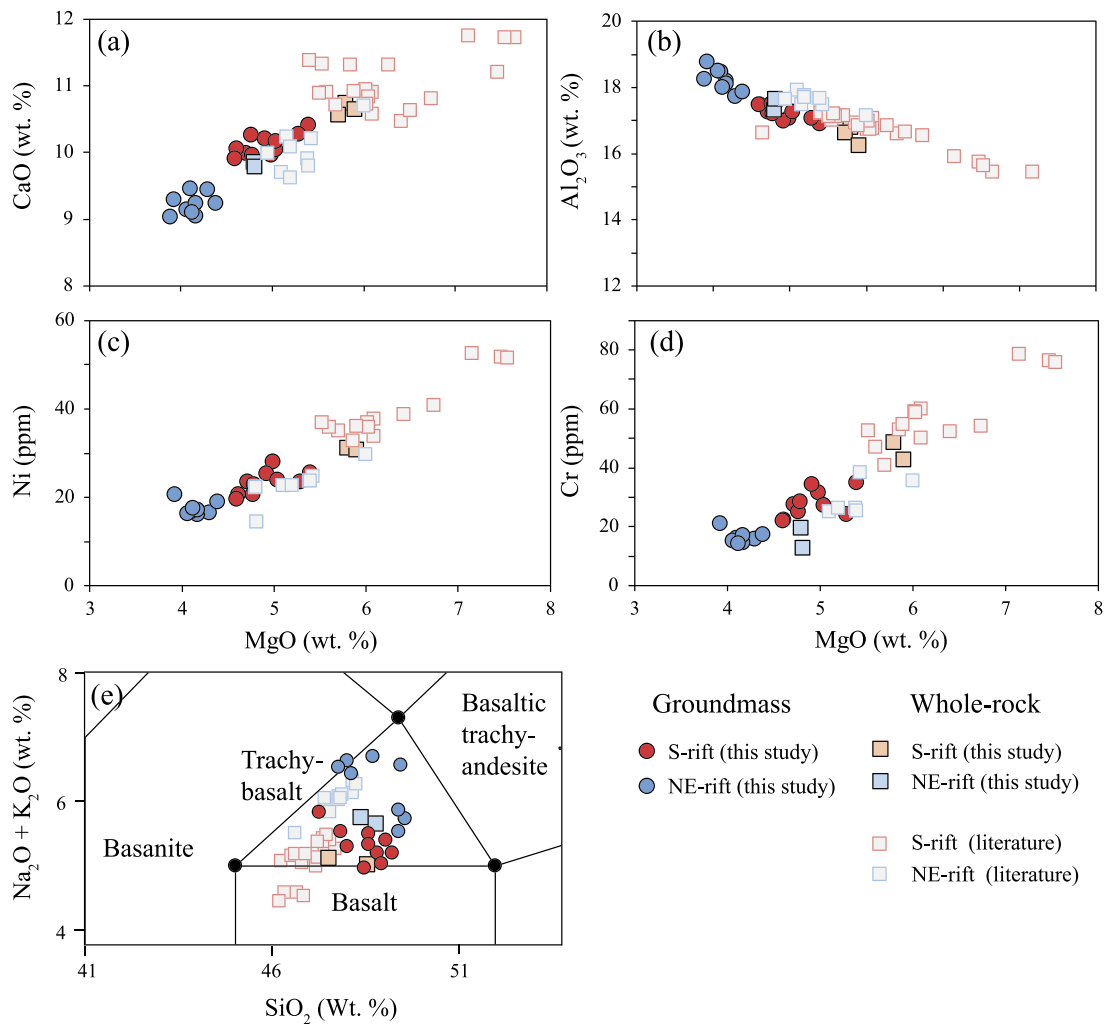
Fig. 2. (a-d) Harker diagrams comparing the composition of whole-rock and groundmass material in NE-rift and S-rift magmas for a selection of major and trace elements. (e) Total alkali-silica diagram (TAS, after Bas et al., 1986) of the same dataset showing that the majority of samples classify as trachybasalts.
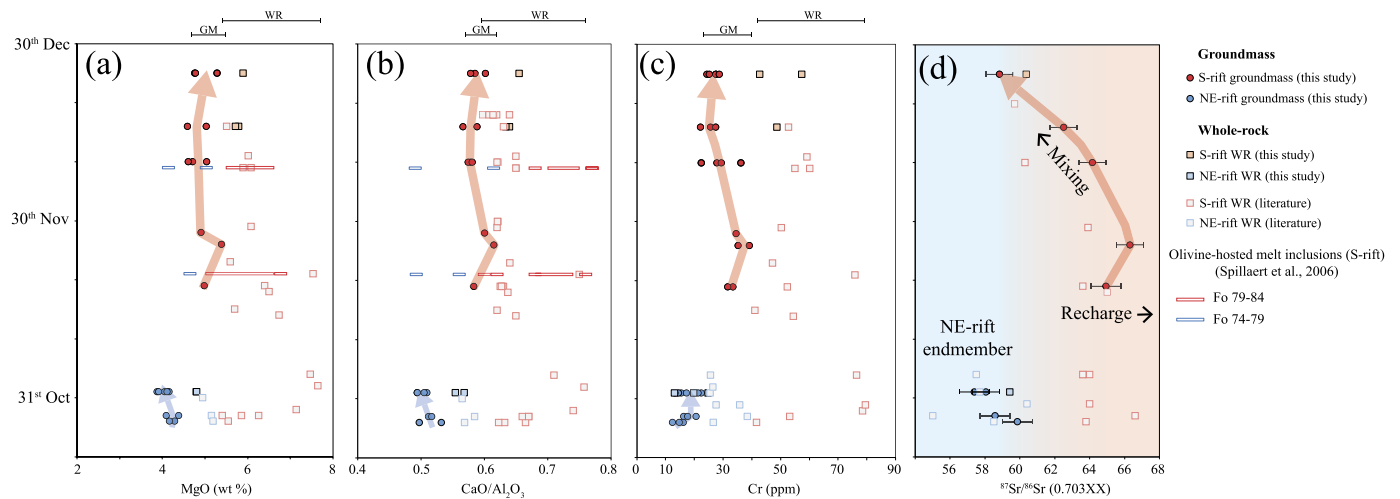
Fig. 3. Chemo-stratigraphies comparing temporal changes in the composition of groundmass, whole-rock (Corsaro et al., 2009; Spilliaert et al., 2006; Viccaro and Cristofolini, 2008; Ferlito et al., 2009; Giacomoni et al., 2012; Di Renzo et al., 2019 and this study) and olivine-hosted melt inclusions (Spilliaert et al., 2006) over the course of the eruption. NE-rift groundmass (blue circles) shows no consistent evolutionary trend, while S-rift groundmass (red circles) shows peaks in (a) MgO, (b) Cr, (c) CaO/Al$_2$O$_3$ and (d) ^{87}Sr/^{86}Sr on the 26th of November, becoming more evolved and less radiogenic thereafter as mixing proceeds. Uncertainties for all major and trace element data from this study are equal to or less than the size of the data point. Error bars denote an uncertainty ($\pm 2\sigma$) of between 8×10^{-6} and 9×10^{-6} for ^{87}Sr/^{86}Sr analysis. The range of values measured in whole-rock material is significantly larger than that of groundmass (a, b and c; ranges shown above plots). Groundmass compositions define a trend intermediate between melt inclusions hosted in the two distinct olivine populations (Fo$_{79-84}$ and Fo$_{74-79}$) found in S-rift magma.

that the porphyricity (crystals >1 mm) of the two analysed whole-rock samples are 3.2 vol. % (sample 302) and 3.7 vol. % (sample 308); meanwhile, other samples show crystal contents of up to 12.4 vol. %, an increase which is mostly reflected in abundance of clinopyroxene. Whole-rock samples that have accumulated varying amounts of mafic phases such as clinopyroxene or olivine will differ markedly in composition (Larrea et al., 2013; Ubide et al., 2014) and can account for much of the range of whole-rock compositions observed in the literature. In the NE-rift, large differences between whole-rock and groundmass composition are also observed (Fig. 2). However, compositional variability is largely equivalent between both datasets suggesting a lack of significant crystal inheritance/accumulation in the whole-rock.

Differences in isotopic composition between whole-rock and groundmass also illustrate the degree to which a crystal cargo is in equilibrium with its host melt. The abundance of antecrysts in a whole-rock sample and more importantly, the composition of the antecrysts themselves (i.e. degree of disequilibrium), determines the extent of isotopic misrepresentation. Negligible differences are observed between the $^{87}Sr/^{86}Sr$ isotope composition of whole-rock and groundmass in NE-rift lavas, indicating that crystallisation occurred in isotopic equilibrium with the host melt. In contrast, groundmass erupted on the S-rift typically shows higher $^{87}Sr/^{86}Sr$ isotope ratios than corresponding whole-rock data from the literature (Fig. 3d), suggesting that the extracted crystal cargo is less radiogenic than its host melt. This observation is supported by isotopic mineral analysis in samples from 1970-2004 which showed that clinopyroxenes were frequently less radiogenic than their corresponding whole-rocks (Armienti et al., 2004, 2007). We note that where both whole-rock and groundmass aliquots of a sample from the S-rift were analysed, the groundmass was in fact slightly less radiogenic than the whole-rock (Fig. 3d). While this appears contradictory, the crystal content of this particular sample (308) is very low (1.6 vol. % clinopyroxene and 1.1 vol. % olivine) and therefore offsets are expected to be small. As the groundmass of this sample is the least radiogenic measured in the S-rift (approximating NE-rift compositions; Fig. 3d), its whole-rock composition is more susceptible to modification by the inheritance of minerals crystallised from the pure eccentric endmember (unsampled, but inferred to be more radiogenic).

5.3. Temporal melt evolution (syn-eruptive processes)

The broad textural and compositional differences between lava emitted on the NE-rift and S-rift (mineral: Fig. 1c, d and melt: Fig. 2) define a baseline relative to which temporal variations within each magma type can be compared across multiple vents on the NE-rift and over a 6-week period on the S-rift.

5.3.1. North-East rift system

The composition of the erupted groundmass is largely equivalent in vents 3b, 3c and 3d, and follows no obvious temporal trend. In fact, compositional variability is greatest within products from the same vent (Fig. 3c), highlighting heterogeneity within erupted products. $^{87}Sr/^{86}Sr$ isotope ratios measured in the groundmass separates of vents 3b-d fall within a narrow range (0.703574 – 0.703599; Fig. 3f), that is distinct from the most radiogenic samples erupted on the S-rift (Di Renzo et al., 2019), but within the range of central-conduit magma erupted between the years 1990 and 2002 (0.703515 – 0.703609; Armienti et al., 2004).

5.3.2. Southern rift system

In contrast, a temporal trend is observed in the composition of groundmass erupted on the S-rift. The earliest erupted products in our dataset (19th Nov – 28th Nov) are the most primitive, distinguished by a large compositional shift relative to magma erupted

on the NE-rift (Fig. 3). However, over the course of the eruption, the compositional gap between the localities is reduced to a minimum of 5 ppm Cr, 0.25 wt. % MgO and 0.2 wt. % Al_2O_3 (10th Dec – 25th Dec) (Figs. 3a, c and B.1d), becoming more evolved over time, in agreement with previous work (Spilliaert et al., 2006; Giacomoni et al., 2012). Notably, when compared with temporally constrained melt inclusions trapped in olivine (Spilliaert et al., 2006), groundmass compositions define a trend intermediate between two populations: those hosted in forsterite <79 and >79 (Fig. 3a, b). This contrasts with whole-rock material which in some cases is more primitive than the most primitive recorded melt inclusion, again highlighting the effect of mineral accumulation (Fig. 3a).

A corresponding temporal shift is clearly reflected in $^{87}Sr/^{86}Sr$ isotope compositions (Fig. 3d). The $^{87}Sr/^{86}Sr$ groundmass ratio peaked on November 26th (0.703663) and became progressively less radiogenic with time (25th December; 0.703588), eventually resembling NE-rift products (Fig. 3f).

### 5.4. Mafic crystal cargo (pre-eruptive processes)

Entire thin section x-ray fluorescence mapping reveals distinct populations of each of the dominant mineral phases: clinopyroxene, olivine and plagioclase. We focus here on processes recorded in the mafic crystal cargo (clinopyroxene and olivine).

5.4.1. Clinopyroxene

A striking difference in clinopyroxene zonation is observed between NE-rift and S-rift lavas. Cr-enrichment at phenocryst rims and in entire microphenocrysts (Fig. 4a), coupled with an increase in MgO within the same zones, was found in 78% of clinopyroxene crystals (n=52) on the S-rift whilst similar enrichments were found in only 16% of NE-rift crystals (n=33) (Fig. 4a inset). This enrichment was described previously by Ubide and Kamber (2018), who carried out targeted LA-ICP-MS trace element mapping on some of the same crystals. In the present study, XFM mapping allows us to observe the occurrence of this enrichment over the course of the eruption and at the entire thin section scale. Although major element compositions of clinopyroxene from the NE- and S-rifts are very similar, some key differences are observed. Large crystals in S-rift samples are punctuated by weak to moderate Cr-enrichment (Fig. 4b) and commonly exhibit sector zoning (Fig. 4c), features that are virtually absent in the NE-rift. In addition, resorbed clinopyroxene cores are distinguished by low manganese concentrations (Fig. 4d), confirming strong disequilibrium between the majority of the crystal and its host melt. Resorbed cores have Na-rich compositions and formed at greater depth (Ubide and Kamber, 2018).

5.4.2. Olivine

Four compositions of olivine were identified in S-rift and NE-rift magmas (Fo_{69-74}, Fo_{74-77}, Fo_{77-80} and Fo_{80-84}) (Fig. 5a-d), which form distinct core and rim zones. In the S-rift the most primitive of these (Fo_{80-84} cores) is the most abundant, comprising 43-73 vol. % of total olivine (Fig. 5e) for each of the three time periods studied, while more evolved olivine (Fo_{74-77} cores; 21-24% and Fo_{69-74} cores; only 2 individual crystals) is uncommon throughout. Notably, the intermediate olivine composition, Fo_{77-80}, forms phenocryst rims and unzoned to weakly-zoned microphenocrysts (0.5-1 mm) that become more abundant over time on the S-rift, increasing from 3 vol. % (November 26th) to 35 vol. % (December 16th) of total olivine. The most abundant olivine compositions in NE-rift products are Fo_{74-77} (41-63 vol. %), and Fo_{77-80} (28-41 vol. %). Primitive Fo_{80-84} is minor in the NE-rift (9-26 vol. %).
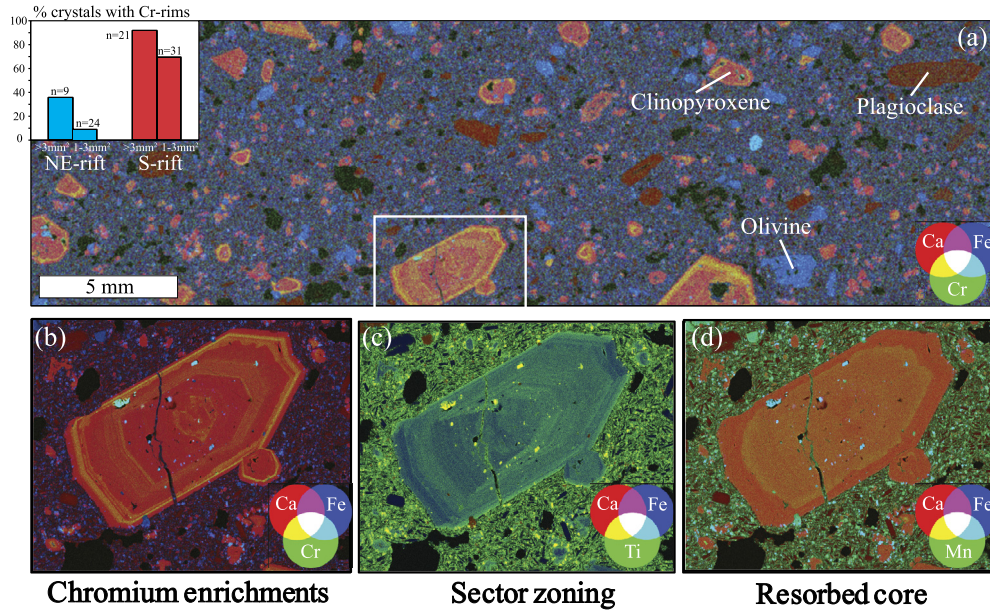
Fig. 4. (a) Three-element XFM map (Ca, Cr and Fe; 10 μm spot size) of S-rift lava, highlighting Cr-rich rims in clinopyroxene crystals (yellow). The inset quantifies the prevalence of Cr-rich clinopyroxene rims in S-rift magma relative to the NE-rift, in which they rarely occur. Panels (b), (c) and (d) show three separate high-resolution maps (2 μm spot size) of the clinopyroxene crystal marked by a white box in panel (a). (b) **Cr**(-Ca-Fe) highlight low-intensity Cr enrichments in the core and mantle of the crystal followed by a high-intensity enrichment (up to 1,000 ppm) at the crystal rim. (c) **Ti**(-Ca-Fe) reveal sector zoning in the crystal. (d) **Mn**(-Ca-Fe) highlight a resorption surface around an inherited core, prior to high Cr-enrichment.
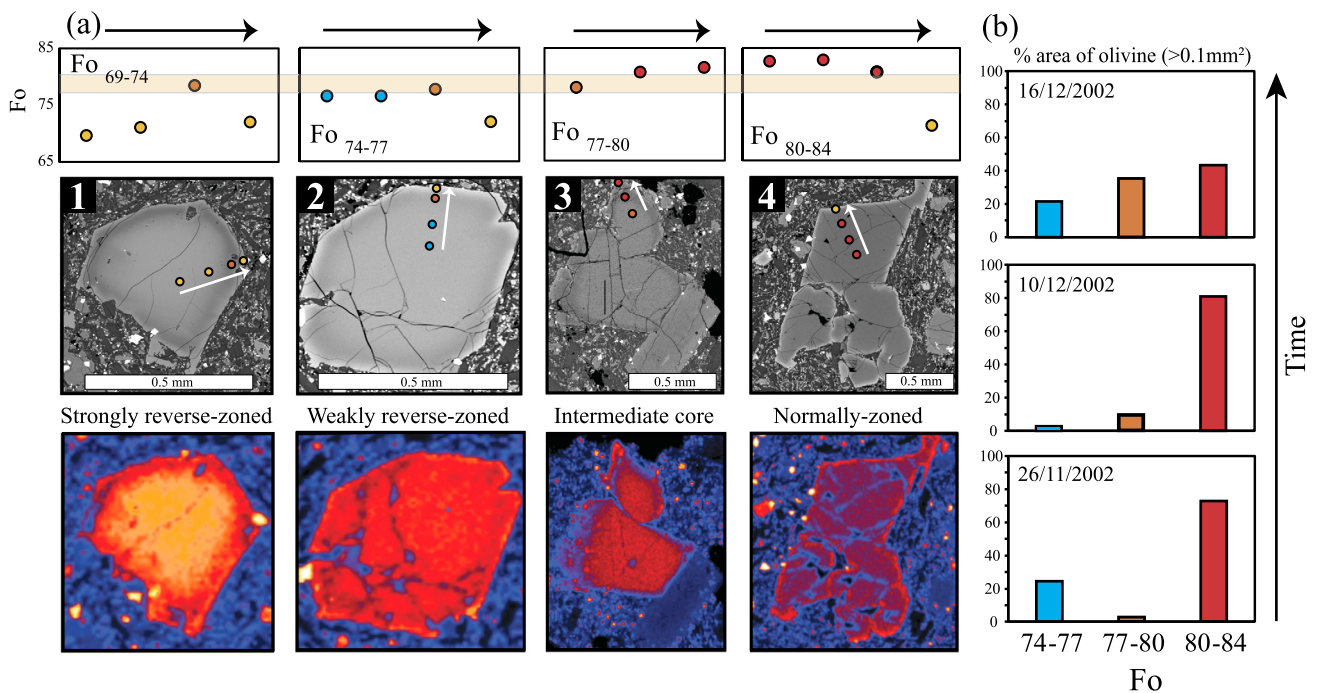
Fig. 5. (a) Olivine populations and zoning patterns in S-rift magma. Four distinct populations (1-4) are shown in XFM compositional maps (Fe concentration from blue-low-to yellow and red-high), back-scattered electron greyscale images and electron microprobe major element transects; Fo_{69-74} (strongly reverse zoned), Fo_{74-77} (weakly reverse zoned), Fo_{77-80} (crystal rims or unzoned microphenocrysts) and Fo_{80-84} (normally zoned). The location of each spot analysis is marked on the back-scattered electron images and arrows indicate analysis order. (b) Histograms representing three different periods of eruption on the S-rift illustrate the changes in the relative abundance of each mineral composition (% area of total olivine >1 mm^2) through time. The most primitive olivine composition (Fo_{80-84}) remains the most abundant throughout, however, the relative abundance of more evolved compositions (Fo_{74-77}, Fo_{77-80}) increases with time. The most evolved olivine, Fo_{69-74}, is not present in significant amounts and is therefore not included in the analysis.

6. Discussion

The separation of mineral (>0.5 mm) and groundmass allows us to track melt evolution as a result of pre-eruptive and syn-eruptive processes, respectively. Groundmass separates from the NE- and S-rifts are sufficiently disparate in elemental and isotopic composition to suggest derivation from separate mantle sources (Fig. 3d) (Clocchiatti et al., 2004; Di Renzo et al., 2019). However, as part of the post-1970 suite of alkali-rich magmas, both melts are some of the most radiogenic ever erupted at Mount Etna, even more radiogenic than the first eccentric magma erupted in 1974 (^{87}Sr/^{86}Sr: 0.703564; Corsaro et al., 2009). To resolve subtle differences between the magmas, we first define their likely characteristics prior to eruption and then examine their syn-eruptive temporal evolution. We then link petrological evidence of magma movement and interaction to monitoring signs, on timescales of days to months.

6.1. S-rift: a hybrid eccentric/central-conduit magma

A close look at the entire S-rift mineral assemblage in thin section-scale XFM maps reveals a mixed crystal cargo along with features of mixing recorded in the minerals themselves (Fig. 4). In our samples, clinopyroxenes record chromium and MgO enrichments at the crystal rim (Fig. 4b), enveloping resorbed crystal cores (Fig. 4d), suggesting an abrupt change in the magmatic environment in the final stages of crystallisation that possibly triggered eruption (see section 6.4). First identified in LA-ICPMS maps of the same crystals (Ubide and Kamber, 2018), this enrichment is observed in 78% of our studied crystals and records the arrival of primitive magma to a more evolved clinopyroxene-bearing resident magma, i.e. magma mixing.

The sense of isotopic offset between groundmass and whole-rock further suggests that much of the S-rift crystal cargo was indeed entrained by a more radiogenic recharge melt. Armienti et al. (2007) measured the ^{87}Sr/^{86}Sr ratios of clinopyroxene phenocrysts erupted during Etna's 2001 lower vents eruption (an eccentric eruption often compared with the 2002-03 S-rift; Clocchiatti et al., 2004) finding that, apart from the outermost rims (removed by acid leaching), the crystals are not in equilibrium with the whole-rock material. More specifically, they found that minerals were less radiogenic than whole-rock compositions and that crystal cores probably originated in earlier melts. This is not surprising given the progressive increase in ^{87}Sr/^{86}Sr ratios documented in central-conduit magmas since 1970 due to mixing with more radiogenic eccentric magma (Armeinti et al., 2004, 2007; Corsaro et al., 2009; Di Renzo et al. (2019)). Only recharge rims and microphenocrysts (Cr-rich clinopyroxene) representing post-mixing crystallisation are likely in equilibrium with (or close to) the true melt (Davidson et al., 2007). Giacomoni et al. (2014) demonstrated that the same is true of plagioclase, finding that only dusty rims were in elemental equilibrium with S-rift whole-rock.

The coexistence of two distinct olivine core compositions, Fo$_{74-77}$ (up to 21% of cores) and Fo$_{80-84}$ (up to 81% of cores), can also be explained by the combination of two magmas each carrying separate crystal cargoes. The more evolved of these core types, like clinopyroxene, is typically resorbed and enveloped by a more primitive rim (core: Fo$_{74-77}$, rim: Fo$_{77-80}$), further corroborating the arrival of primitive recharge magma to a more evolved reservoir. Indeed, clinopyroxene cores and Fo$_{74-77}$ cores are in equilibrium with an overlapping range of melt compositions (Mg# 43-52 and 48-52, respectively; Fig. B.2), pressures (Ol 150-300 MPa; Kahl et al., 2015, Cpx 200-500±200 MPa; this study, Fig. B.3) and water contents (Ol Fo$_{75-78}$ and Cpx Mg# <80: ≤1% H$_2$O; Kahl et al., 2015), typical of Etnean central-conduit magmas. The inclusion of olivine in whole-rock compositions, while having

a significant impact on major element composition, should have little effect on the ^{87}Sr/^{86}Sr isotope composition, given the low abundance of Sr in olivine.

Vertically extensive magma storage is supported by geophysical evidence of a tiered plumbing system (Patanè et al., 2003; Corsaro et al., 2013) in which two established storage regions coincide with crustal discontinuities at approximately 5 ± 2 km and 12 ± 3 km depth (Spilliaert et al., 2006; Giacomoni et al., 2014; Di Renzo et al., 2019). The deeper reservoir is thought to host primitive trachybasaltic melt, while shallowly stored magmas are more evolved on account of degassing and fractionation (Di Renzo et al., 2019 and references therein). Oscillatory low-intensity Cr-zonation observed in the cores of large clinopyroxene crystals (Fig. 4b) may record transfer between deep and shallow central-conduit (low Cr) reservoirs. Sustained interaction within this pathway may have also contributed to the development of hourglass sector-zoning in the same crystals (Fig. 4 b, c). Sector zoning forms in response to low degrees of undercooling (Ubide et al., 2019; Masotta et al., 2020) that can be achieved by slow magma ascent, convection as a response to magma transfer or intrusion, and degassing (Ubide et al., 2019; Klugel et al., 2020). Radiogenic recharge melt is likely buffered to the more dominant central-conduit compositions upon mixing in the shallow plumbing system, accounting for the gradual increase in central conduit ^{87}Sr/^{86}Sr ratios over more than three decades (1970-2002) (Corsaro et al., 2009; Di Renzo et al., 2019).

Normal zoning of more primitive olivine (core: Fo$_{80-84}$, rim: Fo$_{77-80}$), on the other hand, records an opposing crystallisation history. According to MELTS thermodynamic modelling by Kahl et al. (2015), primitive olivine (Fo$_{80-83}$) forms at pressures of 150-300 MPa, temperatures of >1100 °C and, crucially, water contents of 3.5 wt. % equivalent to those measured in the most primitive melt inclusions from S-rift products (3.4 ±0.2 wt. % H$_2$O; Spilliaert et al., 2006). These water-rich conditions are inconsistent with the more evolved mineral phases described above (Kahl et al., 2015) and suggest deep crystallisation prior to significant mixing or degassing in the shallow plumbing system. Melt inclusion entrapment pressures calculated for the same olivine population corroborates crystallisation at depths greater than 10 km (Spilliaert et al., 2006).

The heterogeneity of the crystal cargo (and melts as discussed later) on the S-rift, implies the eruption of a hybrid magma, comprising elements derived from two distinct endmembers (Ferlito et al., 2012; Kahl et al., 2015; Ubide and Kamber, 2018). We suggest that both evolved olivine Fo$_{74-77}$ and the majority of clinopyroxene coexisted in a tiered central-conduit system that was later intruded by a deeply derived, primitive, olivine-bearing eccentric recharge magma. Mixing of these two distinct magmas is recorded by reverse zoning of clinopyroxene and olivine (Fo$_{74-77}$), normal zoning of intruding primitive olivine (Fo$_{80-84}$) and the crystallisation of intermediate/hybrid mineral populations upon mixing. An increase in the prevalence of the intermediate olivine population Fo$_{77-80}$ (forming hybrid crystal cores and microphenocrysts) from 3 to 35 vol. % through time (Fig. 5e) appears to track the progress of post-mixing crystallisation.

Given that mineral populations are inherited from two different magma batches whose isotopic compositions are likely distinct, true changes in melt composition of this mixed magma can only be tracked in the absence of its disequilibrium cargo. Changes in melt composition are discussed in section 6.3.

6.2. The NE rift: unmixed central-conduit magma

Isotopic equilibrium between whole-rock and groundmass in NE-rift magma (Fig. 3d), as well as limited evidence for mixing in the crystal cargo itself, suggests that the majority of minerals crystallised from a similar melt composition (vents 3b-d) (Ferlito et al.,

2009; Giacomoni et al., 2014; Kahl et al., 2015). Unlike the unusually Sr-radiogenic melt erupted on the S-rift (up to 0.70366), the $^{87}Sr/^{86}Sr$ ratios of NE-rift products (0.703574 – 0.703599) resemble those of previously erupted central-conduit magmas (1990-2000; < 0.703515-0.703609; Armienti et al., 2004, 2007). The radiogenic nature of NE-rift magma merely represents a continuation of increasing $^{87}Sr/^{86}Sr$ that began in 1970 (Corsaro et al., 2009; Di Renzo et al., 2019). Only 16% of clinopyroxene crystals on the NE-rift (vents 3b-d) exhibit Cr-enrichments at the crystal rim (an almost ubiquitous feature on the S-rift), whilst olivine populations are largely unzoned. In addition, primitive olivine (Fo_{80-84}) interpreted above as having originated in a recharge magma is rarely found in products of the NE-rift (9-26%). Finally, plagioclase, the most dominant mineral population in NE-rift magma is characterised predominantly by oscillatory zoned textures, attributed either to kinetic effects of crystallisation or minor variations in melt composition (Giacomoni et al., 2014).

These observations, as well as a lack of temporal geochemical evolution in the NE-rift groundmass (melt) from vents 3b to 3d, do not support extensive magma mixing and instead suggest that the NE-rift magma largely escaped interaction with the eccentric endmember, in agreement with many authors who suggested that S-rift and NE-rift magma ascended along separate pathways (Di Renzo et al., 2019 and therein). A small number of Cr-rich clinopyroxene crystals observed in NE-rift products could reflect limited interaction with eccentric products and account for the slightly elevated $^{87}Sr/^{86}Sr$ of the magma relative to earlier central-conduit magmas.

The lack of sector-zoning observed in NE-rift clinopyroxene crystals testifies to storage in a crystallisation environment undisturbed by magma recharge (Giacomoni et al., 2014) where olivine diffusion chronometry records residence times approximating six months (198 ± 109 days; Kahl et al., 2015) and abundant plagioclase phenocrysts reflect storage in the shallow, central-conduit plumbing system (<6 km; Ferlito et al., 2012; Giacomoni et al., 2014). Textural differences between magmas erupted from different NE-rift vents suggest a network of isolated magma batches ponding at various depths, in agreement with the interpretation of Ferlito et al. (2009).

6.3. The syn-eruptive plumbing system; hybridisation through time

Over the course of eruption on the S-rift, the melt composition became increasingly evolved. Following a peak in MgO and Cr on the 26th of November 2002, these key indicators of magma primitivity were progressively depleted (Fig. 3a, c). Although such a compositional shift could occur through fractionation of a common parental magma (Spilliaert et al., 2006; Ferlito et al., 2009; Giacomoni et al., 2012), an accompanying change in $^{87}Sr/^{86}Sr$ isotope composition measured in S-rift groundmass provides strong evidence of magma mixing. Crystallising phases typically retain the isotopic signature of the melt from which they crystallised; thus, any amount of crystal fractionation will have a negligible effect on the $^{87}Sr/^{86}Sr$ ratio of the host melt (Davidson et al., 2007). The observed temporal change is, therefore, interpreted to reflect mixing between two distinct magmas (Fig. 3d, e and f), in good agreement with the mineralogical evidence presented in section 6.1 (Kahl et al., 2015; Ubide and Kamber, 2018).

The maximum difference in $^{87}Sr/^{86}Sr$ melt composition between the S-rift and NE-rift is observed on the 26th of November (Fig. 3d). A S-rift $^{87}Sr/^{86}Sr$ value of 0.70366 marks the most radiogenic melt composition of the entire eruption as well as one of the most radiogenic values measured in Etna's modern history (1624-2005: Clocchiatti et al., 2004; Ferlito et al., 2012). This stark difference progressively diminished over the course of the eruption as the S-rift magma became more evolved and less radiogenic, in-

creasingly resembling and eventually overlapping with that of the central-conduit (as defined by the geochemical characteristics of NE-rift magma), recording progressive hybridisation.

As discussed in section 6.2, central-conduit magma erupted on the NE-rift appears to have been shallowly stored and largely unaffected by magma recharge (Ferlito et al., 2009; Giacomoni et al., 2014). However, the sense of isotopic evolution in hybrid S-rift products (Fig. 3d) is consistent with progressive mixing with a magma akin to that erupted on the NE-rift. Given the ubiquity of central-conduit magma in Etna's plumbing system in the lead up to this eruption (1995-2001 eruptions), multiple pockets of magma with a similar isotopic composition were likely hosted throughout the crustal column (Ferlito et al., 2009; Kahl et al., 2015). In fact, shared textural features (rounded plagioclase cores, Giacomoni et al., 2014) and depths of crystallisation (clinopyroxene barometry; Fig. B.3) in NE-rift and S-rift products, as well as rare quartz-arenite xenoliths found in both magmas (vent 3d, NE-rift), suggest initial storage of central-conduit magmas within a common stratigraphic unit (Fig. 6) (Giacomoni et al., 2012). Upon eccentric recharge, hybrid S-rift magma started to erupt, initially with a stronger eccentric signature and progressively more hybridised with resident central-conduit magma (Fig. 6b). We note that modelling of 1991-2008 olivine populations has pointed to at least 5 distinct magmatic environments within the plumbing system, as shallow as 1.5 km (50 MPa; Kahl et al., 2015). S-rift magma may well have interacted with multiple magma bodies upon ascent, albeit with broadly 'central-conduit' type isotopic compositions. This probably includes early interaction with an amphibole bearing reservoir (Clocchiatti et al., 2004; Ferlito et al., 2012).

While the S-rift hybrid magma is largely devoid of plagioclase, 'ghost-plagioclase' signatures identified in S-rift melt inclusions (Schiavi et al., 2015) suggest that at some point, plagioclase crystallised alongside olivine and clinopyroxene at 5-6 km depth, where H_2O saturation promotes plagioclase crystallisation (Giacomoni et al., 2014). While olivine and clinopyroxene were entrained and retained in the ascending, volatile-rich recharge melt, water-sensitive plagioclase may well have been consumed (Schiavi et al., 2015). We suggest that the fresh input of primitive, volatile-rich recharge magma was compositionally buffered by progressive mixing with degassed central-conduit magma, resulting in the merging of mafic mineral cargoes, hybridisation of melts, growth of intermediate rims (Fig. 6b, inset 4) and dissolution of most pre-existing plagioclase.

It follows that this eruption involved three primary magma bodies: the shallowly stored central-conduit magma erupted on the NE-rift (the central-conduit endmember), a recharge magma (the eccentric endmember, not erupted in pure form) and a hybrid magma resulting from the interaction of eccentric and central-conduit magmas at depth prior to eruption on the S-rift. This model agrees with separate ascent pathways for the S-rift and NE-rift magma (Giacomoni et al., 2012; Di Renzo et al., 2019), but also corroborates evidence of mixing in S-rift magmas identified previously (dusty plagioclase rims, Giacomoni et al., 2014; reverse-zoned olivine, Kahl et al., 2015; reverse-zoned clinopyroxene, Ubide and Kamber, 2018; whole-rock geochemistry, Ferlito et al., 2012). The true $^{87}Sr/^{86}Sr$ composition of the endmember eccentric magma is likely more radiogenic than the most radiogenic groundmass sampled here. Isotopic analysis of melt inclusions hosted in primitive olivine (Fo_{80-84}) may, in future, yield a more representative composition of the original recharge melt.

6.4. Linking petrology, geochemistry and real-time monitoring

Measurable perturbations in seismicity and volcanic gas emissions often precede and accompany volcanic eruption. Contemporaneous variation in melt and mineral chemistry can, however,
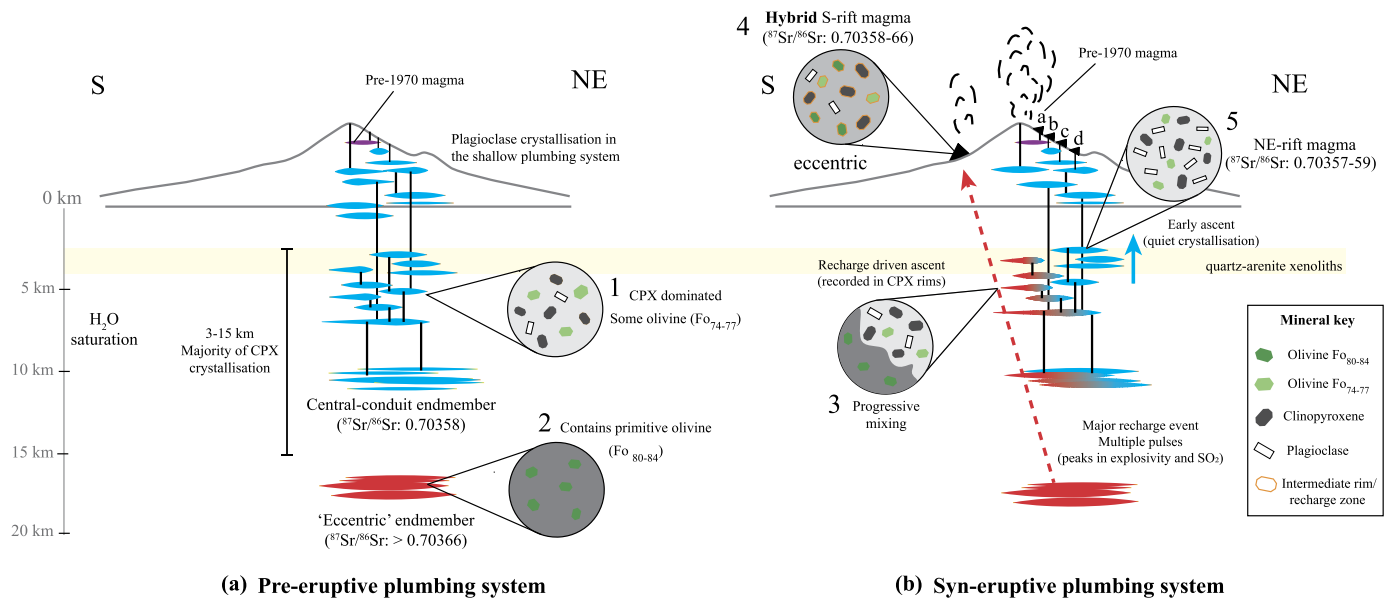
Fig. 6. Two-part conceptual reconstruction of Etna's plumbing system in the lead-up to, and during the 2002-03 eruption. Eccentric and central-conduit endmember magmas are shown in red and blue, respectively. A simplified illustration of the inferred mineral cargo at each stage is illustrated in circular insets (1-5). We note that illustrations are schematic and do not represent true scale or abundance of mineral cargo. (a) The pre-eruptive plumbing system, dominated by central-conduit magma stored in multiple regions (>10 km, 3-5 km and <1 km; Giacomoni et al., 2014) in which polybarically crystallised clinopyroxene (4-15 km; clinopyroxene barometry, Putirka, 2008; Eq. 32b) and olivine (Fo_{74-77}) are the primary mineral phases (inset 1). Recycling of deep clinopyroxene cores (identified from barometry) is not depicted. Eccentric endmember magma is stored in the deep plumbing system (up to 18 km) and hosts a primitive olivine population (Fo_{80-84}) (inset 2). A small batch of pre-1970 magma, identified in products erupted on the upper NE-rift (Ferlito et al., 2009), is shown as a small purple lens in the volcano edifice. (b) Hybridisation of central-conduit and eccentric endmember magmas in the syn-eruptive plumbing system. The dashed red arrow depicts the ascent of eccentric magma from the deep to the shallow plumbing system. Intrusion into, hybridisation and mixing with central-conduit magma is shown as a red-blue gradient. This process resulted in the combination of two distinct mineral cargoes (inset 3) and the subsequent crystallisation of hybrid crystal rims (inset 4). Inset 5 represents magma erupted from vents b-d on the NE-rift. This magma is derived from the central-conduit endmember magma but escaped the effects of mixing with eccentric magma. Protracted residence in the degassing, shallow plumbing system resulted in plagioclase crystallisation and melt evolution.

reveal a wealth of additional information regarding magma storage, transport and eruptive conditions (Gansecki et al., 2019). Geochemical and petrological studies therefore increasingly compliment real-time geophysical monitoring, and inform the interpretation of underlying magmatic processes, both in the lead up to, and during eruption (Kilgour et al., 2014; Rasmussen et al., 2018; Costa et al., 2020).

6.4.1. Pre-eruptive build-up

Following the 2001 eruption at Mount Etna, a period of quiescence ensued during which SO_2 emission was unusually low (< 1,000 t/d) compared with background levels in the era of monitoring (5,300 t/d; Andronico et al., 2005). A significant peak in seismic strain on April 5th 2002 marked the first in a series of microseismic events clustered around 5 km depth (Neri et al., 2005) that, coupled with resumed activity at the summit craters and inflation of the entire volcanic area, was inferred to record renewed refilling of a mid-upper crustal reservoir (Gambino et al., 2004; Patane et al., 2005). In addition, He/Ne ratios (as well as $^3He/^4He$ and He/CO_2) measured at distal degassing sites recorded several peaks indicating the migration of undegassed magma from 10 km to 3-5 km depth (Rizzo et al., 2006). As described in section 6.1 for S-rift products, frequent low-intensity Cr-enrichments in clinopyroxene, as well as polybaric crystallisation and sector zoning may represent the petrological manifestations of magma transfer between tiered 'central-conduit' reservoirs.

Chromium enrichments (up to 1,000 ppm), near-ubiquitous in clinopyroxene crystal rims from the S-rift (Fig. 4a), strongly suggest a recharge-related eruption trigger (Ubide and Kamber, 2018). A deep seismic event (8-18 km), unlike shallow prior activity (clustered at 5 km), was recorded less than 8 weeks before eruption onset, from August 31st to September 3rd (Gambino et al., 2004). This anomalous event has been attributed to the propagation of a

deep magmatic intrusion (Gambino et al., 2004) and is likely the source of the eccentric endmember magma. We speculate that a major peak in the He/Ne ratio (Fig. 7), measured soon afterwards (12th September; Rizzo et al., 2006), heralded the arrival of undegassed eccentric magma to the upper reservoir, where it mixed with resident central-conduit magmas generating zoning patterns in both clinopyroxene and olivine (section 6.1). Indeed, timescales of recharge to eruption calculated based on the thickness of Cr-rich rims in clinopyroxene (2-59 days; Ubide and Kamber, 2018) at an experimentally derived growth rate of 10^{-8} cm/s (Orlando et al., 2008) agree with the onset of mixing approximately 2 months before eruption (see Appendix A.8). Timescales calculated by diffusion chronometry in olivine (44 +-24 days; Kahl et al., 2015) also agree with recharge onset approximately 2 months before eruption. We tentatively suggest that the initial input of recharge magma in early September was subsequently followed by several additional inputs (phase 1 and 2; Fig. 7) that can potentially reconcile the range of timescales recorded by olivine and clinopyroxene. Although no further deep seismicity was recorded prior to eruption, the initial crisis may have opened a pathway through which eccentric magma continued to ascend aseismically, as proposed for the 1999 eruption of Shishaldin volcano, Alaska (Rasmussen et al., 2018). The input of undegassed eccentric magma to the shallow plumbing system likely marks a critical intrusion to a system that was already refilling with central-conduit magma.

In contrast, scant evidence of magma mixing, and the lack of sector-zoned crystals in NE-rift products testifies to a quieter crystallisation environment at conditions close to equilibrium, as suggested from plagioclase chemistry (Giacomoni et al., 2014). These findings are consistent with previous work suggesting that migration of magma in the NE-rift occurred in response to eastward spreading of Etna's eastern flank along the Pernicana fault and was not driven by magma recharge (Neri et al., 2005; Monaco et al.,
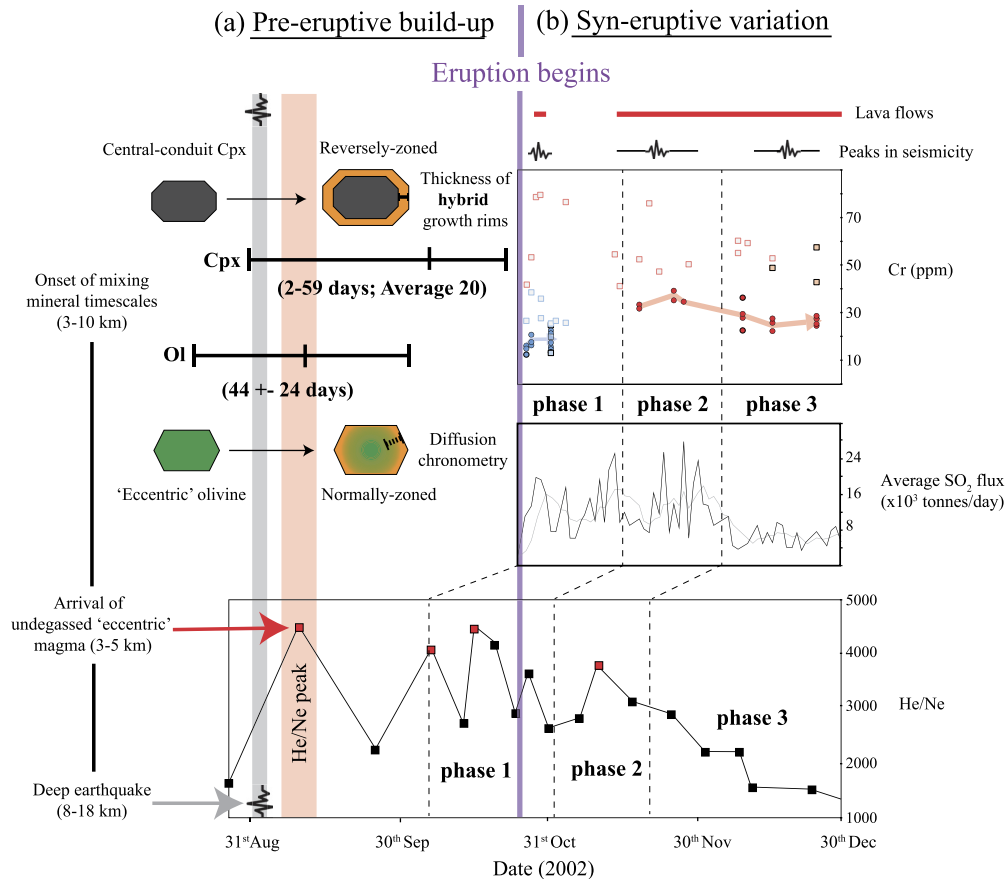
Fig. 7. Comparison of petrological timescales and compositional trends in groundmass (this study) with pre and syn-eruptive monitoring data. The eruption onset is depicted by a vertical purple line. A vertical grey bar indicates anomalously deep earthquake activity (8-18 km) beginning on the 31st of August, 57 days prior to eruption (Gambino et al., 2004) and a vertical red bar marks a peak in the He/Ne ratio (graph redrawn from Rizzo et al., 2006), occurring shortly afterwards indicating the arrival of undegassed magma to the plumbing system. Timescales of recharge to eruption calculated based on the thickness of Cr-rich growth rims (Ubide and Kamber, 2018) and by diffusion chronometry in olivine (Kahl et al., 2015) place the onset of magma mixing in the S-rift at a maximum of 59 and 68 days before eruption onset, respectively. Three distinct phases of activity have been identified during eruption on the S-rift based SO_2 emission (COSPEC measurements; Andronico et al., 2005) and syn-eruptive seismicity (Spilliaert et al., 2006) and are correlated with a similar three phase pattern in the He/Ne ratio (we note that $^3He/^4He$ and He/CO_2 show the same pattern; Rizzo et al., 2006) and chromium composition in S-rift groundmass (phases 2 and 3).

2005). However, we note that overpressure in magmatic storage zones may also have accelerated the spread of the eastern flank (Walter et al., 2005), favouring the onset of eruption.

6.4.2. Syn-eruptive variation

Whereas shallowly stored magma drained from the NE-rift was not replenished, resulting in a short-lived eruption, magmatic supply to the S-rift was sustained by multiple recharge events. Two significant peaks in SO_2 emission and eruption intensity (phases 1 and 2; Fig. 7) are noted during S-rift activity, followed by a steady decline (phase 3; Fig. 7b) until the end of the eruption (Andronico et al., 2005; Spilliaert et al., 2006). Each of these phases is closely associated with seismicity and effusive activity indicative of closed-system, bulk degassing of magma upon ascent (Spilliaert et al., 2006). The first peak occurred at the onset of eruption (Fig. 7 phase 1: 25th Oct – 5th Nov) and was also marked by distinct whole-rock compositions (7.6 wt. % MgO; Fig. 3a and $^{87}Sr/^{86}Sr$: 0.70766; Fig. 3d), interpreted to record the arrival of extremely primitive magma to the plumbing system (Clocchiatti et al., 2004; Giacomoni et al., 2012). We note, however, that Clocchiatti et al. (2004) reported an accumulation of amphibole crystals in the earliest erupted products, attributed to interaction with a shallowly stored hydrous reservoir. Given that whole-rock analyses consistently exaggerate melt primitivity (Figs. 2 and 3), the accumulation of amphibole or other mafic mineral phases could account for the unusually high MgO contents measured in some

early erupted samples. On the other hand, whole-rock analyses typically underrepresent the $^{87}Sr/^{86}Sr$ composition of S-rift melt (Fig. 3d), therefore the high $^{87}Sr/^{86}Sr$ ratio of these early erupted samples does indeed suggest the input of an exceptionally radiogenic melt. The second and largest peak (Fig. 7 phase 2: 20th Nov – 2nd Dec) coincides with the compositional peak identified in this study (26th November; Fig. 3 a, b, c). At this point, the highest SO_2 value ever recorded at Mount Etna, as well as the most primitive and radiogenic groundmass composition, suggest a second input of eccentric magma at depth, midway through the eruption resulting in renewed explosive activity. The final stages of volcanism (phase 3) were characterised by a progressive decline in SO_2 emission, eruption intensity (Andronico et al., 2005; Spilliaert et al., 2006), $^{87}Sr/^{86}Sr$ values and melt primitivity, suggesting not only a waning supply of eccentric magma to the plumbing system, but also progressive mixing with a more undegassed central-conduit magma that can account for similarities with magma erupted from vent 3d of the NE-rift, described by Ferlito et al. (2009).

A strikingly similar pattern is observed in He/Ne ratios (Rizzo et al., 2006 and Fig. 7b). However, each phase occurs approximately 10 days earlier than the geochemical, isotopic and monitoring indices described above. Given a peak in He/Ne is considered to record the arrival of magma at depth (Rizzo et al., 2006), this offset may represent a period of gestation and mixing in the plumbing system prior to ascent and eruption where related peaks in SO_2 and syn-eruptive mixing are subsequently recorded.

7. Conclusions

Considering mineral and melt (hand-picked groundmass) as distinct recorders of magma history, this study reconstructs the pre- and syn-eruptive conditions of Etna's branched 2002-03 eruption. We show that differences in eruption duration and explosivity between two simultaneously erupted magmas are clearly reflected in their respective geochemical characteristics.

Elemental mapping on entire S-rift thin sections reveals a mixed crystal cargo and evidence of magma intrusion recorded in minerals (e.g. reverse zoning of clinopyroxene and olivine), implying the eruption of a two-magma hybrid. Lasting three months, we find that the eruption was sustained by multiple recharge events, tracked closely by variations in melt composition. In contrast, NE-rift magma typical of Etna's post-1970 central-conduit shows scarce evidence of magma mixing, substantiating the view that shallowly stored magma pockets were drained in response to the spreading of Etna's eastern flank.

A multi-disciplinary comparison of pre-eruptive geochemical, petrological and real-time monitoring data identifies the initiation of proximal eruptive build-up ∼2 months before eruption onset. Timescales of recharge to eruption calculated based on olivine and clinopyroxene zoning coincide with deep seismicity and a peak in the He/Ne ratio, likely marking the intrusion of primitive, radiogenic magma to a resident central-conduit reservoir (3-5 km) where progressive mixing is recorded by changes in the $^{87}Sr/^{86}Sr$ isotopic composition. Our results emphasise the potential importance of deep earthquakes as a precursor to highly explosive volcanism, particularly when accompanied by perturbations in volcanic gas emission. However, given differences in the run-up time from deep seismicity to eruption amongst volcanic systems (e.g. 5 to 7 months at Ruapehu, New Zealand; Kilgour et al., 2014) timescales recorded in zoned minerals act as a crucial system-specific constraint.

Most importantly, we demonstrate that analysis of the groundmass fraction resolves clear changes in melt composition relative to whole-rock material, and that the identified geochemical systematics closely reflect eruption dynamics. At present, the time required to conduct such separation and analysis limits this technique to retrospective applications, however, following on from recent petrological monitoring at Hawaii (Gansecki et al., 2019), a move toward rapid high-resolution geochemical analysis may prove useful for hazard response at Mount Etna and active volcanoes globally.

CRediT authorship contribution statement

1. Ruadhán Magee collected, prepared and analysed samples. He interpreted the data, wrote the manuscript and prepared all figures.

2. Dr. Teresa Ubide was instrumental in the project conception and design. She assisted with sample collection, data acquisition and interpretation. Teresa also revised and edited the manuscript.

3. Dr. John Caulfield provided training and assistance with sample preparation and analysis. He also contributed to the interpretation of results and revision of the manuscript.

Declaration of competing interest

The authors declare that they have no known competing financial interests or personal relationships that could have appeared to influence the work reported in this paper.

Funding

Acknowledgements

Appendix. Supplementary material

Supplementary material related to this article can be found online at https://doi.org/10.1016/j.epsl.2021.116904.

References

Andronico, D., Branca, S., Calvari, S., Burton, M., Caltabiano, T., Corsaro, R.A., Del Carlo, P., Garfì, G., Lodato, L., Miraglia, L., Murè, F., 2005. A multi-disciplinary study of the 2002–03 Etna eruption: insights into a complex plumbing system. Bull. Volcanol. 67 (4), 314–330.

Armienti, P., Pareschi, M.T., Innocenti, F., Pompilio, M., 1994. Effects of magma storage and ascent on the kinetics of crystal growth. Contrib. Mineral. Petrol. 115 (4), 402–414.

Armienti, P., Tonarini, S., D'Orazio, M., Innocenti, F., 2004. Genesis and evolution of Mt. Etna alkaline lavas: petrological and Sr-Nd-B isotope constraints. Period. Mineral. 73 (Special issue 1), 29–52.

Armienti, P., Tonarini, S., Innocenti, F., Orazio, M.D., 2007. Mount Etna pyroxene as tracer of petrogenetic processes and dynamics of the feeding system. Spec. Pap., Geol. Soc. Am. 418, 265.

Cashman, K.V., 1992. Groundmass crystallization of Mount St. Helens dacite, 1980–1986: a tool for interpreting shallow magmatic processes. Contrib. Mineral. Petrol. 109 (4), 431–449.

Cashman, K.V., Sparks, R.S.J., Blundy, J.D., 2017. Vertically extensive and unstable magmatic systems: a unified view of igneous processes. Science 355 (6331), eaag3055.

Clocchiatti, R., Condomines, M., Guénot, N., Tanguy, J.C., 2004. Magma changes at Mount Etna: the 2001 and 2002–2003 eruptions. Earth Planet. Sci. Lett. 226 (3–4), 397–414.

Corsaro, R.A., Pompilio, M., 2004. Dynamics of magmas at Mount Etna. Geophys. Monogr., Am. Geophys. Union 143, 91–110.

Corsaro, R.A., Di Renzo, V., Distefano, S., Miraglia, L., Civetta, L., 2013. Relationship between petrologic processes in the plumbing system of Mt. Etna and the dynamics of the eastern flank from 1995 to 2005. J. Volcanol. Geotherm. Res. 251, 75–89.

Corsaro, R.A., Miraglia, L., Pompilio, M., 2007. Petrologic evidence of a complex plumbing system feeding the July–August 2001 eruption of Mt. Etna, Sicily, Italy. Bull. Volcanol. 69 (4), 401.

Corsaro, R.A., Métrich, N., Allard, P., Andronico, D., Miraglia, L., Fourmentraux, C., 2009. The 1974 flank eruption of Mount Etna: an archetype for deep dike-fed eruptions at basaltic volcanoes and a milestone in Etna's recent history. J. Geophys. Res., Solid Earth 114 (B7).

Costa, F., Shea, T., Ubide, T., 2020. Diffusion chronometry and the timescales of magmatic processes. Nature Rev. Earth Environ. 1, 201–214.

Davidson, J.P., Morgan, D.J., Charlier, B.L.A., Harlou, R., Hora, J.M., 2007. Microsampling and isotopic analysis of igneous rocks: implications for the study of magmatic systems. Annu. Rev. Earth Planet. Sci. 35, 273–311.

Di Renzo, V., Corsaro, R.A., Miraglia, L., Pompilio, M., Civetta, L., 2019. Long and short-term magma differentiation at Mt. Etna as revealed by Sr-Nd isotopes and geochemical data. Earth-Sci. Rev. 190, 112–130.

Ferlito, C., Coltorti, M., Cristofolini, R., Giacomoni, P.P., 2009. The contemporaneous emission of low-K and high-K trachybasalts and the role of the NE Rift during the 2002 eruptive event, Mt. Etna, Italy. Bull. Volcanol. 71 (5), 575–587.

Ferlito, C., Viccaro, M., Nicotra, E., Cristofolini, R., 2012. Regimes of magma recharge and their control on the eruptive behaviour during the period 2001–2005 at Mt. Etna volcano. Bull. Volcanol. 74 (2), 533–543.

Ganne, J., Bachmann, O., Feng, X., 2018. Deep into magma plumbing systems: interrogating the crystal cargo of volcanic deposits. Geology 46 (5), 415–418.

Gansecki, C., Lee, R.L., Shea, T., Lundblad, S.P., Hon, K., Parcheta, C., 2019. The tangled tale of Kīlauea's 2018 eruption as told by geochemical monitoring. Science 366 (6470).

Gambino, S., Mostaccio, A., Patanè, D., Scarfi, L., Ursino, A., 2004. High-precision locations of the microseismicity preceding the 2002–2003 Mt. Etna eruption. Geophys. Res. Lett. 31 (18).

Giacomoni, P.P., Ferlito, C., Alesci, G., Coltorti, M., Monaco, C., Viccaro, M., Cristofolini, R., 2012. A common feeding system of the NE and S rifts as revealed by the bilateral 2002/2003 eruptive event at Mt. Etna (Sicily, Italy). Bull. Volcanol. 74 (10), 2415–2433.

Giacomoni, P.P., Ferlito, C., Coltorti, M., Bonadiman, C., Lanzafame, G., 2014. Plagioclase as archive of magma ascent dynamics on "open conduit" volcanoes: the 2001–2006 eruptive period at Mt. Etna. Earth-Sci. Rev. 138, 371–393.

Ginibre, C., Wörner, G., Kronz, A., 2007. Crystal zoning as an archive for magma evolution. Elements 3 (4), 261–266.

Kahl, M., Chakraborty, S., Pompilio, M., Costa, F., 2015. Constraints on the nature and evolution of the magma plumbing system of Mt. Etna volcano (1991–2008) from a combined thermodynamic and kinetic modelling of the compositional record of minerals. J. Petrol. 56 (10), 2025–2068.

Kamenetsky, V.S., Pompilio, M., Métrich, N., Sobolev, A.V., Kuzmin, D.V., Thomas, R., 2007. Arrival of extremely volatile-rich high-Mg magmas changes explosivity of Mount Etna. Geology 35 (3), 255–258.

Kilgour, G.N., Saunders, K.E., Blundy, J.D., Cashman, K.V., Scott, B.J., Miller, C.A., 2014. Timescales of magmatic processes at Ruapehu volcano from diffusion chronometry and their comparison to monitoring data. J. Volcanol. Geotherm. Res. 288, 62–75.

Klügel, A., Day, S., Schmid, M., Faria, B., 2020. Magma plumbing during the 2014-2015 eruption of Fogo (Cape Verde Islands). Front. Earth Sci. 8, 157.

Bas, M.L., Maitre, R.L., Streckeisen, A., Zanettin, B., 1986, IUGS Subcommission on the Systematics of Igneous Rocks. A chemical classification of volcanic rocks based on the total alkali-silica diagram. J. Petrol. 27 (3), 745–750.

Larrea, P., França, Z., Lago, M., Widom, E., Galé, C., Ubide, T., 2013. Magmatic processes and the role of antecrysts in the genesis of Corvo Island (Azores Archipelago, Portugal). J. Petrol. 54 (4), 769–793.

Magee, R., Ubide, T., Kahl, M., 2020. The lead-up to Mount Etna's most destructive historic eruption (1669). Cryptic recharge recorded in clinopyroxene. J. Petrol. 61 (1), egaa025.

Marsh, B.D., 2006. Dynamics of magmatic systems. Elements 2 (5), 287–292.

Masotta, M., Pontesilli, A., Mollo, S., Armienti, P., Ubide, T., Nazzari, M., Scarlato, P., 2020. The role of undercooling during clinopyroxene growth in trachybasaltic magmas: insights on magma decompression and cooling at Mt. Etna volcano. Geochim. Cosmochim. Acta 268, 258–276.

Métrich, N., Allard, P., Spilliaert, N., Andronico, D., Burton, M., 2004. 2001 flank eruption of the alkali-and volatile-rich primitive basalt responsible for Mount Etna's evolution in the last three decades. Earth Planet. Sci. Lett. 228 (1–2), 1–17.

Monaco, C., Catalano, S., Cocina, O., De Guidi, G., Ferlito, C., Gresta, S., Musumeci, C., Tortorici, L., 2005. Tectonic control on the eruptive dynamics at Mt. Etna Volcano (Sicily) during the 2001 and 2002–2003 eruptions. J. Volcanol. Geotherm. Res. 144 (1–4), 211–233.

Neri, M., Acocella, V., Behncke, B., Maiolino, V., Ursino, A., Velardita, R., 2005. Contrasting triggering mechanisms of the 2001 and 2002–2003 eruptions of Mount Etna (Italy). J. Volcanol. Geotherm. Res. 144 (1–4), 235–255.

Rizzo, A., Caracausi, A., Favara, R., Martelli, M., Paonita, A., Paternoster, M., Nuccio, P.M., Rosciglione, A., 2006. New insights into magma dynamics during last two eruptions of Mount Etna as inferred by geochemical monitoring from 2002 to 2005. Geochem. Geophys. Geosyst. 7 (6).

Orlando, A., D'Orazio, M., Armienti, P., Borrini, D., 2008. Experimental determination of plagioclase and clinopyroxene crystal growth rates in an anhydrous trachybasalt from Mt Etna (Italy). Eur. J. Mineral. 20 (4), 653–664.

Patanè, D., De Gori, P., Chiarabba, C., Bonaccorso, A., 2003. Magma ascent and the pressurization of Mount Etna's volcanic system. Science 299 (5615), 2061–2063.

Patane, D., Mattia, M., Aloisi, M., 2005. Shallow intrusive processes during 2002–2004 and current volcanic activity on Mt. Etna. Geophys. Res. Lett. 32 (6).

Putirka, K.D., 2008. Thermometers and barometers for volcanic systems. Rev. Mineral. Geochem. 69 (1), 61–120.

Rasmussen, D.J., Plank, T.A., Roman, D.C., Power, J.A., Bodnar, R.J., Hauri, E.H., 2018. When does eruption run-up begin? Multidisciplinary insight from the 1999 eruption of Shishaldin volcano. Earth Planet. Sci. Lett. 486, 1–14.

Reubi, O., Blundy, J., 2009. A dearth of intermediate melts at subduction zone volcanoes and the petrogenesis of arc andesites. Nature 461 (7268), 1269–1273.

Schiavi, F., Rosciglione, A., Kitagawa, H., Kobayashi, K., Nakamura, E., Nuccio, P.M., Ottolini, L., Paonita, A., Vannucci, R., 2015. Geochemical heterogeneities in magma beneath Mount Etna recorded by 2001–2006 melt inclusions. Geochem. Geophys. Geosyst. 16 (7), 2109–2126.

Spilliaert, N., Allard, P., Métrich, N., Sobolev, A.V., 2006. Melt inclusion record of the conditions of ascent, degassing, and extrusion of volatile-rich alkali basalt during the powerful 2002 flank eruption of Mount Etna (Italy). J. Geophys. Res., Solid Earth 111 (B4).

Steffke, A.M., Harris, A.J., Burton, M., Caltabiano, T., Salerno, G.G., 2011. Coupled use of COSPEC and satellite measurements to define the volumetric balance during effusive eruptions at Mt. Etna, Italy. J. Volcanol. Geotherm. Res. 205 (1–2), 47–53.

Tanguy, J.C., Condomines, M., Kieffer, G., 1997. Evolution of the Mount Etna magma: constraints on the present feeding system and eruptive mechanism. J. Volcanol. Geotherm. Res. 75 (3–4), 221–250.

Ubide, T., Galé, C., Larrea, P., Arranz, E., Lago, M., Tierz, P., 2014. The relevance of crystal transfer to magma mixing: a case study in composite dykes from the Central Pyrenees. J. Petrol. 55 (8), 1535–1559.

Ubide, T., Mollo, S., Zhao, J.X., Nazzari, M., Scarlato, P., 2019. Sector-zoned clinopyroxene as a recorder of magma history, eruption triggers, and ascent rates. Geochim. Cosmochim. Acta 251, 265–283.

Ubide, T., Kamber, B.S., 2018. Volcanic crystals as time capsules of eruption history. Nat. Commun. 9 (1), 1–12.

Viccaro, M., Cristofolini, R., 2008. Nature of mantle heterogeneity and its role in the short-term geochemical and volcanological evolution of Mt. Etna (Italy). Lithos 105 (3–4), 272–288.

Walter, T.R., Acocella, V., Neri, M., Amelung, F., 2005. Feedback processes between magmatic events and flank movement at Mount Etna (Italy) during the 2002–2003 eruption. J. Geophys. Res., Solid Earth 110 (B10).